Nano Energy 90 (2021) 106507

Contents lists available at ScienceDirect

Nano Energy

journal homepage: www.elsevier.com/locate/nanoen

Full paper

Long-term in vivo operation of implanted cardiac nanogenerators in swine

Jun Li [a], Timothy A. Hacker [b,*], Hao Wei [c], Yin Long [a], Fan Yang [a], Dalong Ni [c], Allison Rodgers [b], Weibo Cai [c,*], Xudong Wang [a,*]

[a] Department of Materials Science and Engineering, University of Wisconsin–Madison, Madison, WI 53706, USA
[b] Cardiovascular Research Center, University of Wisconsin-Madison, Madison, WI 53705, USA
[c] Departments of Radiology and Medical Physics, University of Wisconsin-Madison, Madison, WI 53705, USA

ARTICLE INFO

Keywords:
Implantable nanogenerator
Self-powered cardiovascular implantable electronic devices
Long-term implantation
Biocompatibility
Cardiac function

ABSTRACT

Implantable nanogenerators (i-NG) provide power to cardiovascular implantable electronic devices (CIEDs) by harvesting biomechanical energy locally eliminating the need for batteries. However, its long-term operation and biological influences on the heart have not been tested. Here, we evaluate a soft and flexible i-NG system engineered for long-term in vivo cardiac implantation. It consisted of i-NG, leads, and receivers, and was implanted on the epicardium of swine hearts for 2 months. The i-NG system generated electric current throughout the testing period. Biocompatibility and biosafety were established based on normal blood and serum test results and no tissue reactions. Heart function was unchanged over the testing period as validated by normal electrocardiogram (ECG), transthoracic ultrasound, and invasive cardiac functional measures. This research demonstrates the safety, long term operation and therefore the feasibility of using i-NGs to power the next generation CIEDs.

1. Introduction

Among the tremendous efforts to tackle heart diseases, cardiovascular implantable electronic devices (CIEDs) such as pacemakers, cardiac resynchronization therapy (CRT) devices and defibrillators are playing a pivotal role to reduce the morbidity/mortality by monitoring, restoring, and regulating the heart function [1–4]. While these devices perform lifesaving functions, they still possess several limitations that constrain further advancements [5–9]. Conventional CIEDs are rigid and intrinsically incompatible to soft tissues. The batteries required to power the device contributes the majority of the volume and weight, leading to a bulky system with the potential to leak toxic chemicals. Once the batteries are depleted, a second surgery to retrieve and replace the device is necessary, increasing discomfort, the risk of infections, and cost [5,6]. These issues argue for the development of new CIEDs with improved compatibility and innovative energy solutions to last the lifetime of product.

Nanogenerator (NG) holds great promises in enabling self-powering abilities [10–18]. Implantable nanogenerators (i-NGs) have been designed to overcome these limitations [19–26]. Using i-NGs to harvest energy directly from the beating heart has the potential to eliminate batteries [27–37]. In fact, the newest generation of i-NGs can produce power up to ~33 μW, matching the power consumption of many CIEDs [31,32]. Indeed, the output current density of some high-performance i-NGs could exceed the membrane potential of cardiomyocytes thus triggering a contraction (0.377 μJ) [33]. This would allow an i-NG to directly stimulate heart beats [38]. The latest generation of membranous i-NGs can be manufactured to mimic the softness and flexibility of tissues, leaving tissue function unchanged [39–41]. However, this burgeoning i-NG technology is still far from clinical applications. Current studies are primarily focused on device innovation and demonstrating performance parameters [42–45]. Most reported on-heart i-NGs were only tested for a few hours under an open-chest environment [34]. Practical applications of i-NGs would require matching the lifetime of i-NGs to today's CIED's which can last up to 10 years and have excellent tissue compatibility [6,43]. In order to bring the promising i-NG technology to clinical applications, one critical and urgent question yet to be answered is its long-term in vivo operation and its physiological influences on heart function and systemic and local biocompatibility[53].

To address this critical need, here we developed a soft and flexible i-NG with a set of specially designed leads and receivers enabling monitoring of the in vivo operation of epicardially-implanted NGs without opening the chest. In this study, an i-NG was implanted on the epicardium of swine hearts for 2 months. Blood chemistry and tissue pathology

* Corresponding authors.
E-mail addresses: th2@medicine.wisc.edu (T.A. Hacker), WCai@uwhealth.org (W. Cai), xudong.wang@wisc.edu (X. Wang).

https://doi.org/10.1016/j.nanoen.2021.106507
Received 23 June 2021; Received in revised form 22 August 2021; Accepted 6 September 2021
Available online 11 September 2021

analysis demonstrated good biocompatibility. Heart function was unchanged over the course of the study as shown by a lack of changes in electrocardiogram (ECG), cardiac function and structure as measured by transthoracic ultrasound and cardiac pressure–volume loop analysis. This research will serve as a firm underpinning for the feasibility and safety of long-term on-heart implantation and operation of i-NGs.

2. Materials and methods

2.1. I-NG system fabrication and characterization

A 5 nm chromium (Cr) layer and 50 nm gold (Au) layer were deposited on both sides of ~40 μm PVDF film (PolyK Technologies, LLC, Philipsburg, PA, USA.) as electrodes by E-beam Evaporator (CHA-600). The gold deposited PVDF film was cut into a 1.5 cm × 2 cm piece, with four small holes (~2 mm in diameter) drilled by micro drill press at each corner. After connected with Au-coated tungsten (W) wires (0.1 mm diameter) purchased from VWR International LLC, a 15–20 μm Parylene-C thin film was deposited on both sides of PVDF and Au-coated W wires as the first package layer using a parylene chemical deposition system (Model 3000 Lab Top, PARA Tech Coating, Inc.). A second layer package of i-NG was received by casting PDMS (Sylgard 184, Tow Corning) solution consisting of pre-mixed elastomer and crosslinker at the ratio of 10–1 with different thickness (400 μm on one side, 800 μm theother side). The Au-coated W wires were packaged with ~ 2 mm PDMS by casting and molding. The receiver connecting another side of W wires was made of an aluminum plate (10 × 10 mm^2) embedded within molded button-shaped silicone with a size of 15 × 15 × 7 mm^3.

Driven by a computer-controlled actuator (LinMot), the piezoelectric voltage outputs of i-NG were measured by connecting probes of a low-noise voltage preamplifier (Stanford Research Systems, model SR560) to the top and bottom electrodes. The short-circuit current outputs were measured by a low-noise current preamplifier (Stanford Research Systems, model SR570) connected with LabVIEW system in computer. The bending moduli and dynamic moduli of PDMS, PVDF and i-NG were measured by a dynamic mechanical analyzer (Rheometrics Solids Analyzer III) through a three point-bending test and a frequency sweeping test, respectively.

2.2. Cytotoxicity study

2.2.1. Cell morphology and immunofluorescence staining

After 3T3 cells were cultured on the films (PVDF, PDMS, Parylene-C) or in 24-well plates (control group), the cell morphology was observed directly using a confocal microscope (Nikon A1RS HD Confocal Microscope). The cytoskeleton and nucleus were stained with Flash Phalloidin™ Green 488 (BioLegend) and blue fluorescent Hoechst (352/461 nm) (Thermo Fisher Scientific), respectively. Reconstitute the Flash Phalloidin™ Green 488 with 1.5 ml of methanol to make 300 units stock solution. The samples were fixed with 2–4% formaldehyde for 15 min and then rinsed three times with prewarmed phosphate-buffered saline (PBS). The samples were incubated with Flash Phalloidin™ Green 488 (diluting 300 μL stock solution 1:50 in 1X PBS) and Hoechst (50 nM) for 30 min at 37 °C. After staining, the cells were rinsed with prewarmed buffer three times and samples imaged using a Nikon A1R HD Upright Multi-Photon/Confocal microscope.

2.2.2. MTT assay

NIH 3T3 fibroblasts (HUVECs, CAMBREX) were cultured in a complete growth media comprised of high glucose modified Eagle medium (DMEM) with L-glutamine, supplemented with 15% fetal bovine serum (Hyclone; Thermo Fisher Scientific). The cells were seeded into 96-well culture plates with different films, maintained at 37 °C in a humidified atmosphere in the presence of 5% CO_2, and the culture medium was changed every day. After up to 4 days, MTT (3-(4,5-dimethylthiazol-2-thiazolyl)−2,5-diphenyl-2 H-tetrazolium bromide) assay (ThermoFisher Scientific) was performed to examine cell viability. MTT solution (100 μL) was added to each well. After 4 h of incubation, the medium was removed, and DMSO (500 μL/well) was added to dissolve the precipitated fomazan. The optical density (n = 3) of the solution was evaluated using a microplate spectrophotometer at a wavelength of 490 nm.

2.3. I-NG implantation and in vivo performance

All animal experiments were conducted under a protocol approved by the University of Wisconsin Institutional Animal Care and Use Committee. Briefly, domestic male and female adult swine (~30 kg) were sedated with intramuscular Telazol (4 mg/kg) and xylazine (2 mg/kg) and then intubated and ventilated with a respirator and anesthetized with isoflurane (2%) and oxygen. Ventilation was adjusted to maintain blood gases in the physiological range. Animals were monitored continuously for anesthetic state by jaw tension, heart rate, blood pressure, end-tidal CO_2 and oxygen saturation. A surface electrocardiogram (ECG) was monitored through a veterinary monitor system (BM5VET, Bionet) during the entire procedure. A mini-thoracotomy was then performed to implant the i-NG between the heart and pericardium. The leads from the device were tunneled and the receivers were placed subcutaneously on the animals back. The dependence of i-NG output on heart rate was studied with heart rates controlled by a temporary pacemaker (Grass SD9 stimulator) or injecting Dobutamine (2–20 mcg/kg/min IV). The voltage outputs of implanted i-NG were measured by penetrating needle probes connected with a low-noise voltage preamplifier (Stanford Research Systems, model SR560) into the receivers. The short-circuit current outputs were measured by a low-noise current preamplifier (Stanford Research Systems, model SR570). All animals were fed normally after the implantations. Standard postoperative care including analgesia was given to animals until they were active and could eat normally.

2.4. Biocompatibility and biosafety assessment

Blood and serum tests were performed prior to implantation (0 week) and at 2 weeks, 4 weeks, and 8 weeks post-implantation. Blood samples were taken at each time point after the animals were sedated as above with telazol and xylazine. For histological analysis, animals were euthanized at the end of study, tissue around NG, together with tissues from vital organs (kidney, liver, lung, and spleen) were collected for histological analysis. The tissue was fixed in 10% formalin and sectioned at 10 μm thickness. Tissue sections were hematoxylin and eosin (H&E) stained for analysis.

2.5. Evaluation of cardiac functions

Domestic adult swine (~30 kg) were sedated, ventilated and anesthetized, and monitored as above. The surface electrocardiogram (ECG) was monitored through a veterinary monitor system (BM5VET, Bionet) prior to implatation and at 2, 4, and 8 weeks post-implantation. Cardiac structure and function were measured by transthoracic ultrasound (Vivid Q, G.E.Healthcare) at the same time as the ECG measurements. Pressure volume loop analysis was performed prior to implantation and at 8 weeks post implantation. A 5Fr pressure-volume catheter (Transonic, NY) was inserted through a 6Fr sheath placed in either in the right carotid artery or femoral artery and advanced to the LV. Percutaneous access of the right femoral vein was obtained and 10Fr shearth was placed. A 32 mm balloon (Coda LP Cook Medical) was pushed through the sheath and advanced to the inferior vena cava with the tip just cadual to the RA. Baseline LV pressures and volumes were recorded and then the venous balloon was briefly inflated to alter loading conditions on the heart. This was repeated 3 times and the data recorded for later analysis. For survival animals, catheters and sheaths were removed and wounds closed and animal recovered. Eight weeks post implant, pressure-volume analysis was repeated as above and the animals were

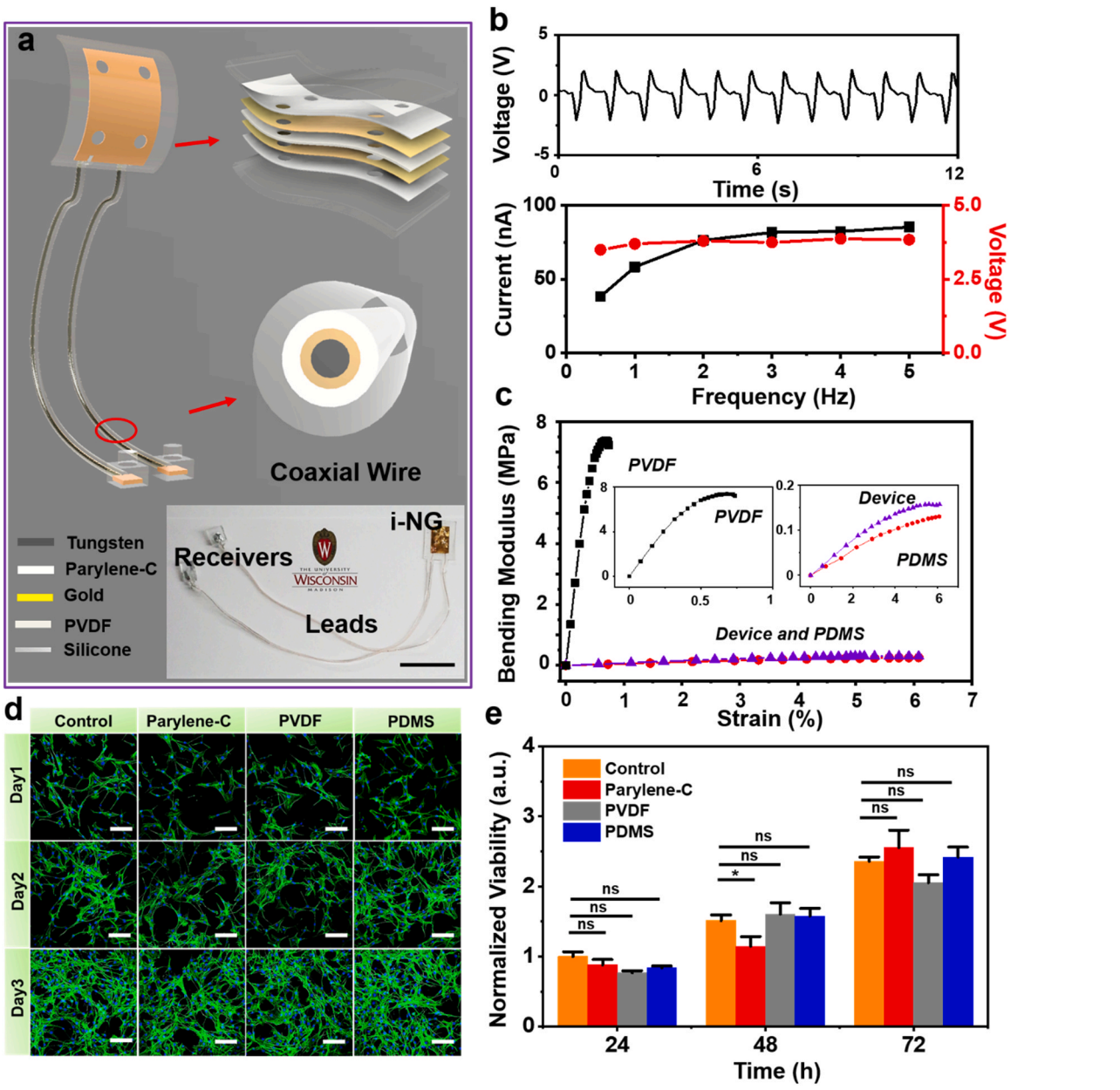

Fig. 1. I-NG fabrication and characterization. (a) Schematics of a flexible i-NG consists of the i-NG component, a pair of coaxial leads, and receivers. (b) In vitro electrical outputs of a packaged i-NG bent by a computer-controlled actuator. (c) Bending moduli of i-NG devices in comparison to PVDF and PDMS. (d) Viability of cells cultured on top of different films/substrates as a function of time. The control group refers to cells cultured in a culture dish. The scale bar is 50 μm. (e) Fluorescence microscope image of 3T3 fibroblast cells cultured on top of different films/substrates. Data are expressed as mean ± SD (n = 6). The *p < 0.05 (statistically significant) and ns = not significant.

euthanized and the hearts were removed and examined grossly for signs of infection.

3. Results and discussions

A flexible i-NG was designed and fabricated based on piezoelectric polymer, gold-coated polyvinylidene fluoride (PVDF) with a thickness of 40 μm. As shown in the Fig. 1a, the complete system consisted of three components, the i-NG component, a pair of coaxial leads, and receivers. All the components are hermetically packaged by encapsulating the device in a thin layer of Parylene C (~20 μm) and a relatively thick layer of polydimethylsiloxane (PDMS) (~1.2 mm). Gold standard silicone and parylene insulating materials prevented the leakage current of device. Together with soft and flexible piezoelectric polymer, they guaranteed the biosafe operation of i-NG over long-term implantation. Coaxial wire consisting of tungsten core and gold shell was selected because of the robust mechanical property of tungsten and the excellent electrical conductivity of gold. The receiver had an aluminum plate (10 × 10 mm^2) embedded within molded silicone. The thick silicone packages were button-shaped with a size of 15 × 15 × 7 mm^3. To acquire electric output from i-NG, the needle probes were pushed through the silicone package to make contact with the gold plates.

The performance of packaged i-NG was first characterized in vitro. A computer-controlled actuator bent the i-NG at a frequency of 1 Hz (at a bending radius of approximately 1 cm), creating a peak-to-peak voltage (V_{pp}) of ~3.8 V and peak-to-peak current (I_{pp}) of ~60 nA (Fig. 2b). The outputs were due to the excellent ferroelectricity of the PVDF film (Fig. S1a). When the actuation frequency varied from 0.5 to 5 Hz (the

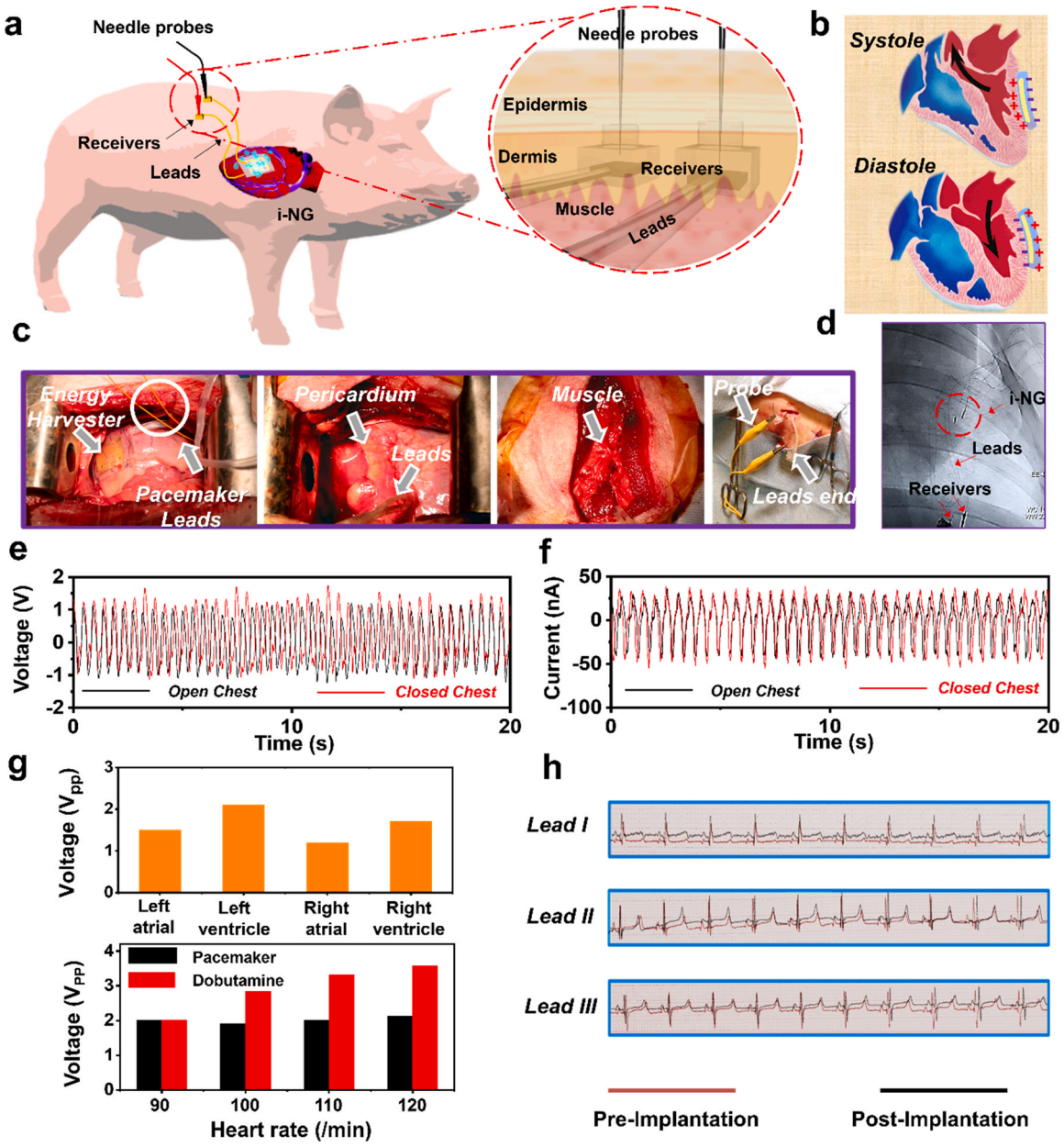

Fig. 2. Implantation of designed i-NG system and its in vivo performance. (a) Schematics of the whole i-NG system placed in swine, with output signals measured by penetrating needle probes through skin. (b) The schematic working mechanism of i-NG on heart. (c) Implantation procedures of the i-NG system. (d) X-ray image revealing the implanted i-NG system. (e) The voltage outputs of i-NG under both open chest and closed chest conditions. (f) The current outputs of i-NG under both open chest and closed chest conditions. (g) The influence of implantation sites the cardiac contractility on device outputs. The top panel is the voltage outputs on different implantation sites and the bottom panel is the voltage outputs as a function of heart rate. (h) ECG signals of swine pre-implantation and post-implantation.

typical frequency range of biomechanical movement), the voltage output remained stable at 3.8 V. However, I_{pp} increased from 38 nA to 85 nA as the frequency increased, which may be attributed to a faster charge induction between electrodes. Considering the out-of-plane polarization of the PVDF film, a planar electrode configuration was advantageous as compared to interdigitated electrodes because they maximize piezoelectric charge collection under the same stimulations (Figs. S1b and 1c). Due to the thick PDMS package being used, the device incorporating a thin PVDF film (40 μm) exhibited a low bending modulus of 3.64 MPa, close to pristine PDMS (Fig. 2c and Fig. S1d). Therefore, this i-NG could conform to the heart muscle tissues.

Biocompatibility of the components of the i-NG were tested by culturing 3T3 rat fibroblast cells (RFCs) on the top of each layer (PVDF, Parylene C and PDMS). Immunofluorescence staining was performed after culturing for three-days examining cell attachment, morphology, and proliferation. As presented in Fig. 1d, all RFCs after of 1 day of culturing had a low density but well adhered to all films with typical cellular morphology. After 2–3 days of incubation, the RFCs exhibited normal behavior and reached a higher density with a typical filamentous and stretched morphology. The cell morphology, distribution and densities did not show significant dissimilarity between the experiment and control groups. Cell viability was tested by 3–(4,5–dimethylthiazol-2–yl)-2,5–diphenyltetrazolium bromide (MTT) assay (Fig. 1e). The groups were not significantly different compared to the control group therefore demonstrating the materials are non-toxic.

The i-NG system was then implanted in adult swine (Fig. S2a) and its in vivo performance was assessed. As shown in Fig. 2a, the i-NG component was implanted on the epicardium of the swine heart (left

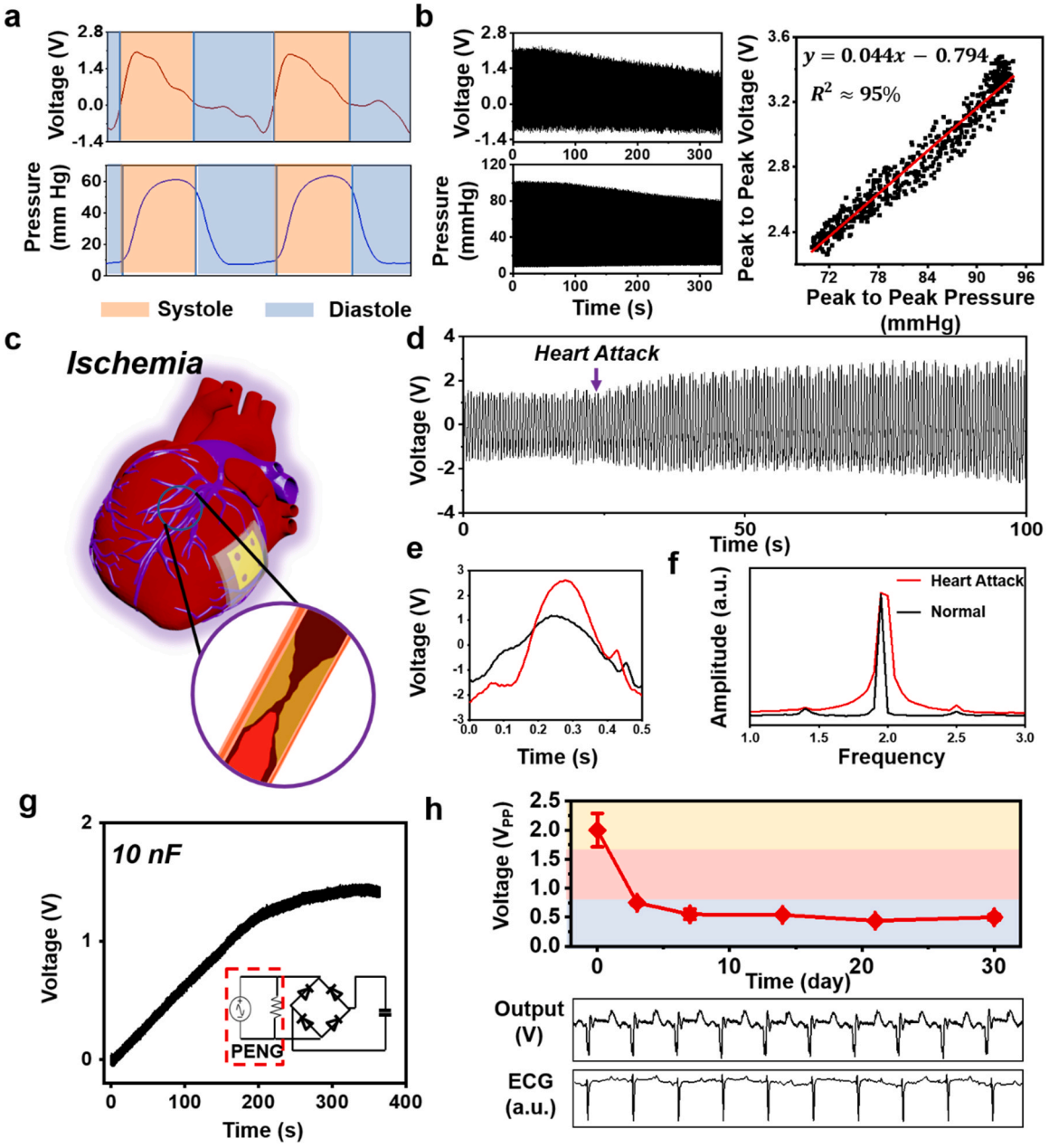

Fig. 3. Multi-functions of i-NGs with a long-term stability. (a) Simultaneous measurements of voltage outputs of device and pressure inside the LV. (b) The variation in voltage output in response to the pressure change. The correlation between V_{pp} and peak to peak pressure reveals an excellent linearity ($R^2 \approx 95\%$). (c) Schematics of cardiac ischemia by blocking the coronary artery. (d) Voltage outputs of i-NG under normal heartbeat and heart attack (e) Comparison of single voltage envelopes from (d). (f) The fast Fourier transformation (FFT) of the outputs shown in (d). (g) Charge a 10 nF capacitor by the implanted i-NG harvesting heart biomechanical energy. (h) Long-term stability evaluation of i-NG over 30 days. The bottom panel is the comparison of i-NG outputs and corresponding ECGs.

ventricle area) with the coaxial leads passing through the ribs and tunneling under the skin to the back of swine. The receivers were affixed between the dermis layer of the skin and muscles by sutures. The output signals of i-NG could be measured by pushing the needle probes through the skin and silicone cover and reaching the aluminum patches inside. Removal of the needle probes allowed the elastic silicone cover to reseal, preventing the infiltration of biofluids and short circuit or erosion of the device. The use of the penetrating needle probes through skin to access the i-NG is a minimally invasive approach that is capable of providing a long-term in vivo monitoring of the device performance. The elastic receiver design supported multiple measurements without observable property decay.

A schematic of the working mechanism of i-NG is presented in Fig. 2b. During systole, the heart contracts so that the PVDF film bends inward. A potential difference is generated between the two electrodes (bottom and up sides of PVDF films) due to the deformation. When the heart expands during diastole, the PVDF film is bent outward and produces an opposite potential.

The implantation procedure is illustrated in Fig. 2c. A mini-thoracotomy was performed first to visualize the left ventricle (LV) after opening the pericardium layer. The i-NG was sutured (Fig. S2b and Movie S1) onto the LV epicardial wall. The pericardium, ribs and muscle layer were closed. The leads were tunneled and placed subcutaneously on the animal's back. Two needle probes connected with a voltage meter were used to test the device. The implanted system was observed by X-ray, as revealed in Fig. 2d.

Supplementary material related to this article can be found online at doi:10.1016/j.nanoen.2021.106507.

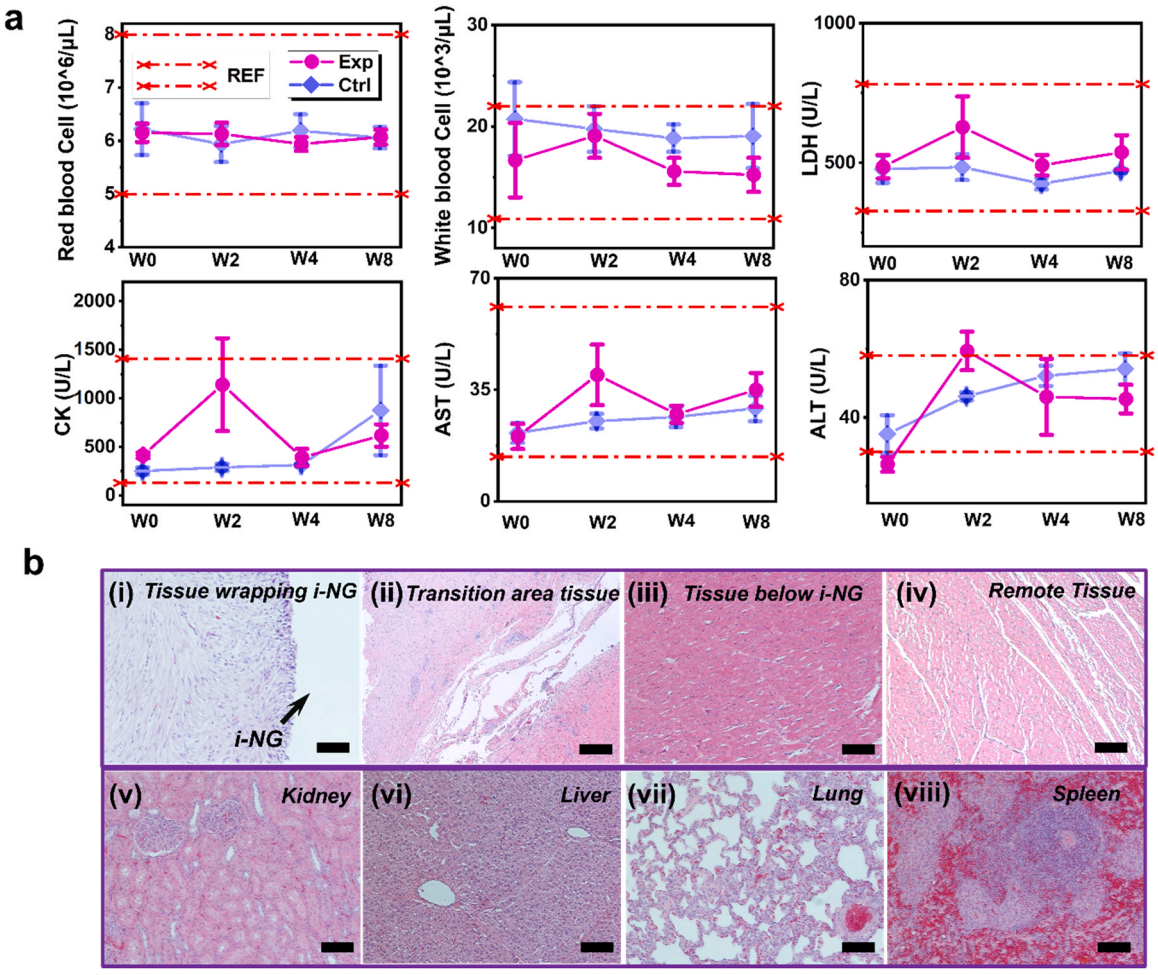

Fig. 4. Long-term biocompatibility evaluation. (a) Blood and serum tests results. Experiment group (N = 4) are the pigs implanted with i-NGs. Control group (N = 4) are the pigs without i-NG implantation. The normal range is marked in between two orange dashed lines. Red blood cell (RBC) and white blood cell (WBC) are indicators of hematopoietic function and infection, respectively. Alanine aminotransferase (ALT), aspartate aminotransferase (AST), creatine kinase (CK), and lactate dehydrogenase (LDH) are the common cardiac enzymes to evaluate heart function. (b) pathological analyses by H&E staining of regional tissues surrounding the implanted device (i)-(iv) and on most vital organs, such as (v) kidney, (vi) liver, (vii) lung, and (viii) spleen.

The outputs of embedded device were examined during implantation (open chest) and afterwards (closed chest). The implanted i-NG produced a V_{pp} of approximately 2.1 V under the open chest condition (Fig. 2e). When the swine chest was closed, the V_{pp} slightly increased to 2.3 V, possibly due to increased thoracic pressure. Analogously, the current was boosted from ~ 68 nA (open) to 77 nA (closed). In separate experiments, different implantation sites were tested, including left atria (LA), LV, right atria (RA), and right ventricle (RV) (Fig. 2g). LV yielded the highest output of 2.1 V, followed by RV of 1.7 V. The higher output of the ventricles over atria is due to the larger ventricular movement. As a further test, swine were dosed with dobutamine (15 mcg/kg/min) (increases cardiac contraction strength and heart rate), and the outputs of the i-NG were measured (Fig. 2g and Fig. S2c). At a heart rate of 120/min, the V_{pp} reached ~ 3.6 V. To determine if the increase in V_{pp} was due to increases in heart rate or contractility, we altered heart with an external pacemaker. V_{pp} did not change at either higher or lower heart rates. Electrocardiogram (ECG) traces were collected pre and post device implantation to examine the safety of the implanted device. No abnormal heart rhythm (arrhythmias) was noted at any time during the implantation period, suggesting that device does not interfere with heart electrical activity. (Fig. 2h and Fig. S3).

The output of i-NG was measured simultaneously with LV pressure (Fig. 3a). During systole, LV pressure increases dramatically to pump the blood from chamber into the arteries which produces an upward voltage envelope. As the cardiac pressure drops during diastole, the i-NG generates a downward voltage signal. Next, blood flow to the heart was altered by briefly inflating a 32 mm balloon (Coda LP Cook Medical) in the inferior vena cava just caudal to the RA. As less blood was returned to the heart due to the balloon occlusion, LV pressures dropped with corresponding changes in the voltage output (Fig. 3b). The correlation between V_{pp} and peak to peak pressure is plotted in right panel of Fig. 3b, demonstrating excellent linearity ($R^2 \approx 95\%$) with a slope of 44 mV mm Hg^{-1}. Moreover, correction between V_{pp} and other important cardiac parameters such as ejection fraction (EF), heart power, and cardiac output (Fig. S4) were also observed.

Since the i-NG device immediately tracked changes in heart performance, it could be used to monitor heart function in real time. To demonstrate this potential, we temporality occluded the left anterior descending (LAD) artery causing ischemia, similar to what would happen during a heart attack [46,47] (Fig. 3c). In the cardiac ischemia, both T-wave and ST segment in ECG showed abnormality, with the T-wave reversed and the ST segment elevated (Fig. S5). The i-NG immediately responded to the ischemia with an increase in V_{pp} to ~ 4.5 V from an average of 2.3 V under normal conditions (Fig. 3d). The increase was because initially the heart beat more powerfully in an attempt to overcome the ischemia (Fig. 3e). Moreover, a fast Fourier transformation (FFT) of the output revealed that the voltage signals during heart attack had a broad peak distribution compared to the peaks

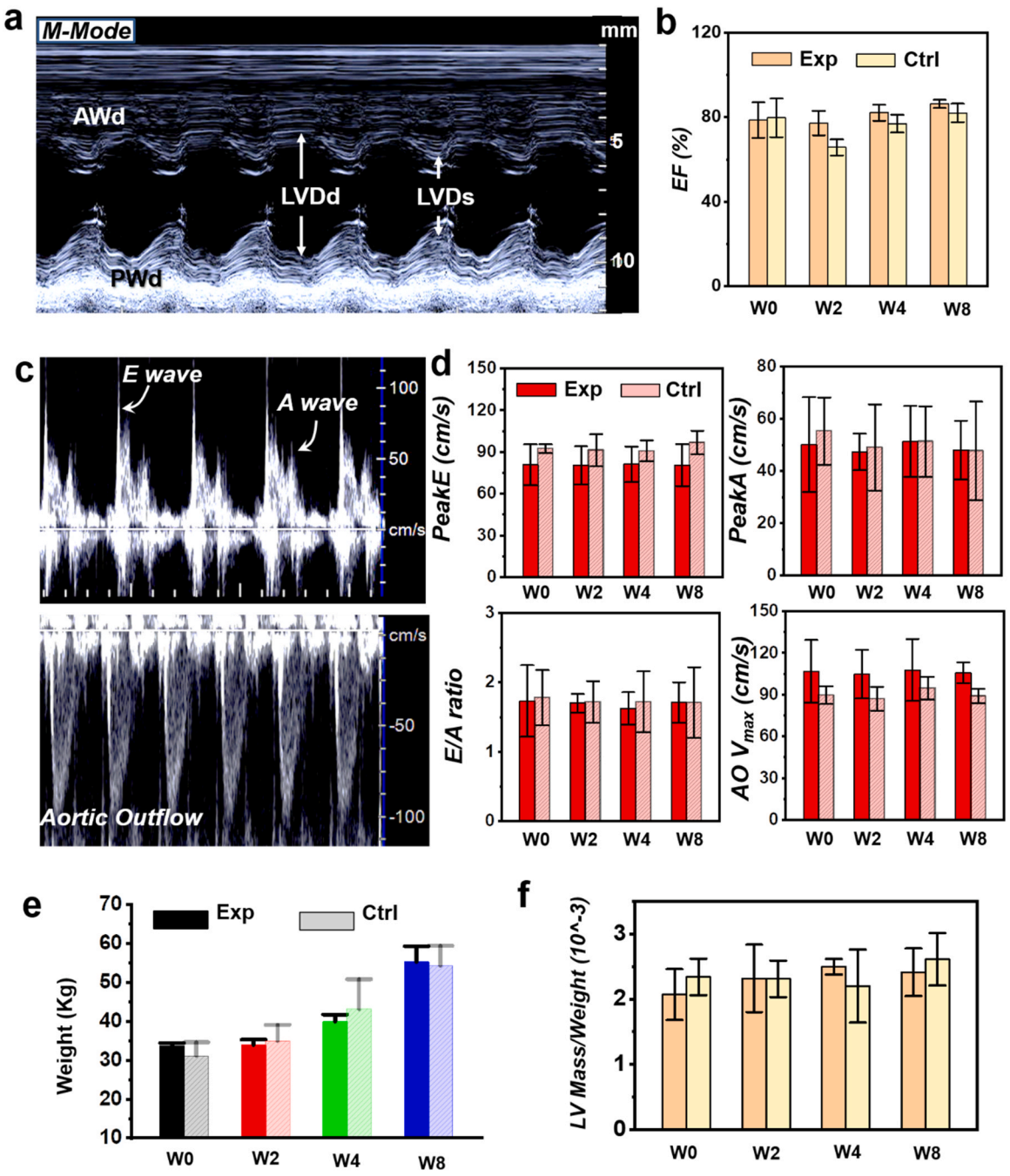

Fig. 5. Long-term heart functions evaluated by transthoracic ultrasound. (a) Two-dimensional motion-mode (M-mode) imaging showing the movement of LV. (b) The contractility of heart as a function of time, represented by ejection fraction (EF). (c) The Doppler ultrasound signals of blood flow though mitral valve and aortic valve. (d) Measured blood flow velocities, including peak velocities of E wave and A wave, E/A ratio and max aortic flow velocity, as a function of time. (e) The change of swine weight during the two-month period. (f) The change of LV mass to body weight ratio over the whole implantation period.

under normal conditions (Fig. 3f), which were the result of more irregular movements. In addition to real-time surveillance, this device could also effectively harvest the biomechanical energy from regular heart beats to powering other electronics. Fig. 3g shows that the i-NG could charge a 10 nF capacitor to 1.5 V in 5 min driven by heartbeats.

To evaluate the long-term in vivo operation of the i-NG, the output of i-NG was recorded for one month, when the swine was under a normal life. It was demonstrated in Fig. 3h that the implanted device kept active during the entire implantation period. However, there was a fast drop from 2.0 V (V_{pp}) to approximately 0.75 V in the first three days after implantation, while afterwards the output remained relatively stable and leveled off at ~0.5 V (Fig. S6a). Since the output power and efficiency are directly related to the voltage output, they follow the same trend as the voltage during the implantation (Section 2, Supporting Information). The initial drop in voltage may be attributed to the encapsulation of the device with connective tissue given the hydrophobic surface of device favorable for the protein adsorption and cell adhesion. On recovery of the device 8 weeks post-implantation the device was intact, however, a thin layer of tissue encapsulated the device, which could significantly degrade the device performance due to restriction of its movement (Fig. S6b and S6c). Meanwhile, it was clearly observed that the waveform of device output was altered and became synchronized with ECG waveform after 2 weeks (Fig. 3h and Supporting Movie S2), as compared to the broad voltage envelopes on the first few days.

Table 1
LV wall thickness and chamber dimensions measured by echocardiography. LVDd, LVDs, ADW, and PDW stand for LV dimension during systole, LV dimension during diastole, anterior wall thickness in diastole, and posterior wall thickness during diastole, respectively.

Groups		Structural Parameters			
		LVDd (mm)	LVDs (mm)	ADW (mm)	PDW (mm)
Exp	Pre	33.6 ± 1.5	19.9 ± 3.0	6.3 ± 0.6	6.3 ± 0.5
	Week 2	35.5 ± 2.9	21.7 ± 3.2	6.8 ± 1.0	6.8 ± 1.0
	Week 4	38.0 ± 2.1	21.4 ± 2.6	8.1 ± 1.0	8.0 ± 1.1
	Week 8	40.7 ± 1.7	21.0 ± 1.1	8.7 ± 1.0	8.5 ± 1.0
Ctrl	Pre	37.3 ± 1.5	19.3 ± 2.9	5.3 ± 0.6	6.0 ± 0.1
	Week 2	39.7 ± 1.5	25.3 ± 1.5	5.7 ± 0.6	5.7 ± 0.6
	Week 4	38.3 ± 2.1	21.3 ± 0.6	6.7 ± 0.6	5.7 ± 0.6
	Week 8	41.0 ± 2.6	20.7 ± 2.5	8.0 ± 0.1	8.7 ± 0.6

This synchronization may be due to the tissue encapsulation causing the device to more accurately respond to heart movement. Although the encapsulation affected the device output, it did not damage the device. Once removed from the animal, the device was re-tested in vitro and it achieved the same output as prior to implantation (Fig. S7), confirming its durability. In addition, ECG performed at different time frames exhibited no abnormal reading, indicating normal heart rhythm (Fig. S8).

Supplementary material related to this article can be found online at doi:10.1016/j.nanoen.2021.106507.

Blood and serum analysis were performed on two groups of swine models (N = 4 for each group) during the implantation period to evaluate biocompatibility and biosafety of the implanted devices (Fig. 4a). Each swine in the experiment group received the i-NG implantation, while the control group only had the mini-thoracotomy without any device implantation. There was no evidence of infection based on stable values in white blood cells (WBC) throughout the evaluation period. Hematopoietic function as measured by red blood cell (RBC) also remained steady for both groups during the entire testing period. Major WBCs like neutrophils, lymphocytes, monocytes, and basophil, all stabilized within the normal range (Fig. S9). Enzymes, particularly biomarkers of cardiac tissue damage, were fully examined. The common cardiac enzymes to evaluate heart function including alanine aminotransferase (ALT), aspartate aminotransferase (AST), creatine kinase

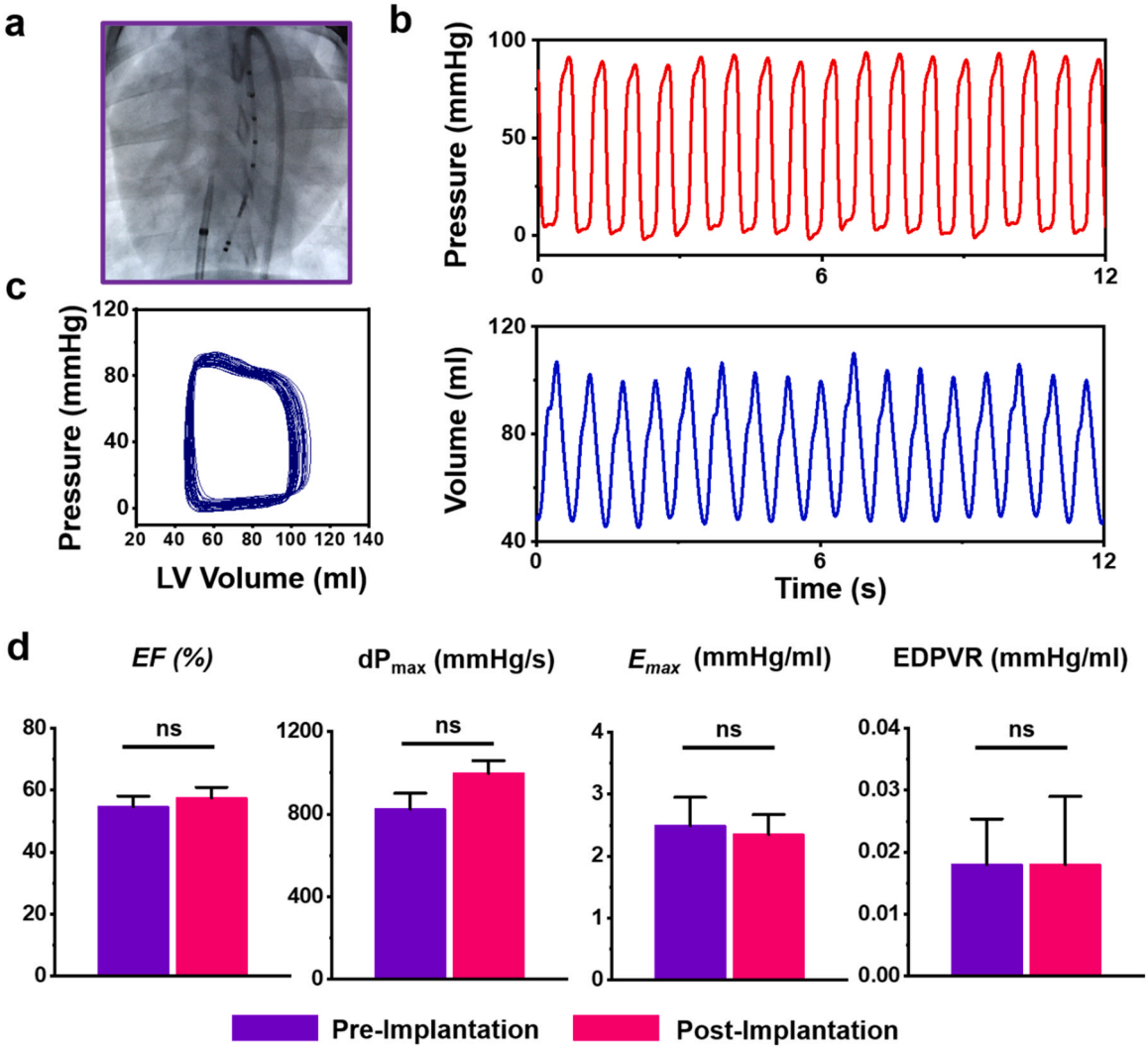

Fig. 6. Evaluation of cardiac functions and cardiac mechanics. (a) X-ray image of advancing an invasive PV catheter to the left ventricle. (b) Real-time LV pressure and volume measured by the catheter. (c) PV loops by plotting the LV pressure against LV volume at multiple time points during a complete cardiac cycle. (d) Comparisons of typical indicators related to heart functions derived from the PV loops prior implantation and post implantation. Ejection fraction (EF) represents the fraction of blood ejected from LV within each contraction. The dP_{max}/dt is the maximum rate of pressure change in the ventricle. E_{max} represents the peak LV elastance while the slope of end-diastolic PV relationship (EDPVR) indicates the LV stiffness. Data are expressed as mean ± SD. The *p < 0.05 (statistically significant) and ns = not significant.

Table 2
LV volume/pressure parameters measured by PV loop. HR, SV, SW, and CO stand for heart rate, stroke volume, stroke work, and cardiac output, respectively.

Groups		Volume/Pressure Parameters			
		HR	SV (ml)	SW (J)	CO (ml min^{-1})
Exp	Pre	93.7 ± 15.0	49.3 ± 4.4	0.6 ± 0.1	4803.2 ± 1170.0
	Week 8	85.5 ± 6.8	98.4 ± 9.5	0.9 ± 0.1	8812.7 ± 1680.0
Ctrl	Pre	97.4 ± 0.3	44.0 ± 6.5	0.39 ± 0.1	4345.7 ± 637.9
	Week 8	97.3 ± 2.9	69.0 ± 5.1	0.69 ± 0.1	6794.0 ± 274.0

(CK), and lactate dehydrogenase (LDH) were all moderately elevated directly following the surgery (at the second week) in the experiment group, yet all returned to normal after 4 weeks. The initial elevation might be related to the suturing the device to the heart or the wounds created to access the heart. Troponin I, a cardiac muscle protein regulating the muscular contraction, [48–50] was also assessed (Fig. S9). This protein was at a low level over the entire period, indicating there was no cardiac muscle damage. In addition, pathological analyses to diagnose the potential infections and necrosis were performed after the animals were euthanized (week 8) by harvesting the tissues. Regional tissues surrounding the implanted device were sectioned and stained by Hematoxylin and eosin (H&E) staining first, as shown in Fig. 4bi-iv. There were no obvious infiltrations of lymphocytes in the adjacent tissues and neither tissue injury nor morphological change at muscular cells were observed, coinciding with the blood test results. The formation of fibrous capsule around the device was confirmed by the observed dense fibroblasts, indicating a mild foreign body reaction at early stage. Pathological tests were conducted on most vital organs, including heart, lung, liver, spleen, and kidney as well. All the organs showed no deformation or abnormal lymphatic cell invasion, further confirming all the swine remained in good health throughout the experiment.

The long-term heart function was also evaluated during the implantation period by echocardiography (Fig. S10). Heart function was unchanged over the implantation period. Ejection fraction (EF), as measured from m-mode images (Fig. 5a), indicates the ability of the heart to pump blood was unchanged over the course of the study (Fig. 5b). Doppler ultrasound was used to measure blood velocity through the mitral and aortic valves (Fig. 5c). These velocities were in the normal range, stable throughout the testing period and not different between groups (Fig. 5d). The E/A ratio of blood velocities through the mitral value were unchanged during the study and not different between groups indicating normal diastolic function. Likewise, velocities through aortic valve were in the normal range and not different between groups for the duration of the study. Cardiac structure was measured from m-mode images and was not different between groups. Wall thickness and chamber dimensions increased over the course of the experiment (Table 1) as the pigs grew from an average starting body weight of 33.73–55.27 kg (Fig. 5e) by the end of the study. Therefore, the LV mass to body weight ratio remained constant demonstrating no significant changes in cardiac structure during the implantation period.

Left ventricular cardiac function was also evaluated with a pressure-volume (PV) catheter (Fig. 6a), pre and 8 weeks post device implantation. PV analysis is the gold standard to measure cardiac function [51, 52]. Real-time LV pressure and volume were directly measured by the sensors in catheter, as shown in Fig. 6b, showing the regular pressure and volume variation during cardiac cycles. Pressure-volume loops are displayed by plotting the LV pressure against LV volume during the cardiac cycle (Fig. 6c). Pressures and volumes obtained from these loops were unchanged between groups and over the course of the experiment except due to growth of the animal (Table 2).

Cardiac function as measured by EF, matched well with the transthoracic ultrasound results, over the course of the experiment. There was no significant variation in the maximal rate of pressure increase during contraction (dP_{max}/dt, an index of ventricular performance) during the same period (823.26 mmHg/s pre-implantation vs. 998.25 mmHg/s post-implantation). Load-independent LV functional parameters were also studied and did not show any difference with device implantation. E_{max} representing the peak LV elastance did not show a significant variation (< 6%) post implantation. Similarly, the LV stiffness, obtained by the slope of end-diastolic PV relationship (EDPVR), was almost unchanged with only approximately 1% variation. Similar results were found in E_{max} and EDPVR in the control group before and 8 weeks after surgery. (Fig. S11 and Table 2). Therefore, the invasive but precise PV loop analyses revealed no change in cardiac function over time and thus the safety of the implanted nanogenerator.

4. Conclusion

In summary, a cardiac i-NG system was developed and implanted on swine hearts over a period of 2 months. The i-NG implanted on the LV epicardium produced greatest voltage output as compared to RV, RA or LA. The output correlated well with changes in cardiac contractility (R^2 = 95%), which could potentially enable real-time detection of heart diseases such as ischemic heart attack. The i-NG would be able to provide enough electric energy to power small electronics. During the implantation period, this system triggered a mild foreign body reaction but continued to produce a stable electrical output. The device did not cause any significant damage or infection to the heart tissues based on the cardiac enzymes and tissue staining analysis. Cardiac structure was also unchanged as measured by echocardiography. LV function was unchanged over the course of the experiment and not different from sham animals as evaluated by echocardiography and invasive pressure-volume analysis. This research validates the long-term safe implantation and operation of cardiac i-NG system over a two-month period. Although two-month study is relatively short compared to the lifetime of today's CIED's that can last up to 10 years, the stable performance of i-NG together with very mild reactions over the whole course of studies could reflect much longer expected lifetime, indicating a first advance that filled the blank in this field. It marks an important advance for soft and flexible self-powered cardiac systems toward clinical applications.

CRediT authorship contribution statement

Jun Li: Conceptualization, Methodology, Validation, Visualization, Data curation, Writing – original draft. **Timothy A Hacker:** Methodology, Validation, Data curation, Supervision, Writing – review & editing. **Hao Wei:** Methodology, Validation. **Yin Long:** Methodology, Validation. **Fan Yang:** Methodology, Visualization. **Dalong Ni:** Methodology, Validation. **Allison Rodgers:** Methodology. **Weibo Cai:** Supervision, Writing – review & editing. **Xudong Wang:** Conceptualization, Supervision, Writing – review & editing, Funding acquisition.

Declaration of Competing Interest

The authors declare that they have no known competing financial interests or personal relationships that could have appeared to influence the work reported in this paper.

Acknowledgement

This publication was supported by the National Institute of Biomedical Imaging and Bioengineering of the National Institutes of Health under Award Number R01HL157077. The content is solely the responsibility of the authors and does not necessarily represent the official views of the National Institutes of Health. Jun Li is grateful for the support of Johnson Controls fellowship. The authors thank Everett Temme for providing help with tissue sectioning and staining.

Appendix A. Supporting information

Supplementary data associated with this article can be found in the online version at doi:10.1016/j.nanoen.2021.106507.

References

[1] M.M. Steffen, J.S. Osborn, M.J. Cutler, Cardiac implantable electronic device therapy permanent pacemakers, implantable cardioverter defibrillators, and cardiac resynchronization devices, Med. Clin. North Am. 103 (2019) 931–943.

[2] F.A. McAlister, J. Ezekowitz, N. Hooton, V. Ben, C. Spooner, D.M. Dryden, R. L. Page, M.A. Hlatky, B.H. Rowe, Cardiac resynchronization therapy for patients with left ventricular systolic dysfunction - a systematic review, Jama J. Am. Med. Assoc. 297 (2007) 2502–2514.

[3] S.K. Mulpuru, M. Madhavan, C.J. McLeod, Y.M. Cha, P.A. Friedman, Cardiac pacemakers: function, troubleshooting, and management part 1 of a 2-part series, J. Am. Coll. Cardiol. 69 (2017) 189–210.

[4] H.G. Mond, A. Proclemer, The 11th world survey of cardiac pacing and implantable cardioverter-defibrillators: calendar year 2009–a world society of arrhythmia's project, Pacing Clin. Electrophysiol. 34 (2011) 1013–1027.

[5] S. Richter, M. Doring, M. Ebert, K. Bode, A. Mussigbrodt, P. Sommer, D. Husser, G. Hindricks, Battery malfunction of a leadless cardiac pacemaker worrisome single-center experience, Circulation 137 (2018) 2408–2410.

[6] J. Dean, N. Sulke, Pacemaker battery scandal, BMJ 352 (2016) 228.

[7] J. Res, J. de Priester, A. van Lier, C. van Engelen, P. Bronzwaer, P. Tan, M. Visser, Pneumothorax resulting from subclavian puncture: a complication of permanent pacemaker lead implantation, Neth. Heart J. Mon. J. Neth. Soc. Cardiol. Neth. Heart Found. 12 (2004) 101–105.

[8] A. Chauhan, A. Grace, S. Newell, D. Stone, L. Shapiro, P. Schofield, M. Petch, Early complications after dual chamber versus single chamber pacemaker implantation, Pacing Clin. Electrophysiol. 17 (1994) 2012–2015.

[9] D. Bhatia, S. Bairagi, S. Goel, M. Jangra, Pacemakers charging using body energy, J. Pharm. Bioallied Sci. 2 (2010) 51–54.

[10] Z.L. Wang, J. Chen, L. Lin, Progress in triboelectric nanogenerators as a new energy technology and self-powered sensors, Energy Environ. Sci. 8 (2015) 2250–2282.

[11] C.S. Wu, A.C. Wang, W.B. Ding, H.Y. Guo, Z.L. Wang, Triboelectric nanogenerator: a foundation of the energy for the new era, Adv. Energy Mater. 9 (2019).

[12] M. Wang, J.H. Zhang, Y.J. Tang, J. Li, B.S. Zhang, E.J. Liang, Y.C. Mao, X.D. Wang, Air-flow-driven triboelectric nanogenerators for self-powered real-time respiratory monitoring, ACS Nano 12 (2018) 6156–6162.

[13] S.X. Xiang D.J. Liu, C.C. Jiang, W.M. Zhou, D. Ling W.T. Zheng, X.P. Sun, X. Li, Y.C. Mao, C.X. Shan, Liquid-Metal-Based Dynamic Thermoregulating and Self-Powered Electronic Skin, Advanced Functional Materials.

[14] Y.K. Liu, W.L. Liu, Z. Wang, W.C. He, Q. Tang, Y. Xi, X. Wang, H.Y. Guo, C.G. Hu, Quantifying contact status and the air-breakdown model of charge-excitation triboelectric nanogenerators to maximize charge density, Nature Commun. 11 (2020).

[15] S.F. Hao, J.Y. Jiao, Y.D. Chen, Z.L. Wang, X. Cao, Natural wood-based triboelectric nanogenerator as self-powered sensing for smart homes and floors, Nano Energy 75 (2020), 104957.

[16] M.Y. Gao, P. Wang, L.L. Jiang, B.W. Wang, Y. Yao, S. Liu, D.W. Chu, W.L. Cheng, Y. R. Lu, Power generation for wearable systems dagger, Energy Environ. Sci. 14 (2021) 2114–2157.

[17] Y. Zou, L. Bo, Z. Li, Tailored mesoporous inorganic biomaterials: assembly, functionalization, and drug delivery engineering, Adv. Mater. 33 (2021), 2005215.

[18] H. Feng, C. Zhao, P. Tan, R. Liu, X. Chen, Z. Li, Nanogenerator for biomedical applications, Adv. Healthc. Mater. 7 (2018), 1701298.

[19] J. Li, X.D. Wang, Research update: materials design of implantable nanogenerators for biomechanical energy harvesting, APL Mater. 5 (2017), 073801.

[20] H.J. Yoon, S.W. Kim, Nanogenerators to power implantable medical systems, Joule 4 (2020) 1398–1407.

[21] Y. Long, J. Li, F. Yang, J.Y. Wang, X.D. Wang, Wearable and implantable electroceuticals for therapeutic electrostimulations, Adv. Sci. 8 (2021), 2004023.

[22] R. Hinchet, H.J. Yoon, H. Ryu, M.K. Kim, E.K. Choi, D.S. Kim, S.W. Kim, Transcutaneous ultrasound energy harvesting using capacitive triboelectric technology, Science 365 (2019) 491–494, 491-+.

[23] J. Li, L. Kang, Y.H. Yu, Y. Long, J.J. Jeffery, W.B. Cai, X.D. Wang, Study of long-term biocompatibility and bio-safety of implantable nanogenerators, Nano Energy 51 (2018) 728–735.

[24] Z. Liu, H. Li, B.J. Shi, Y.B. Fan, Z.L. Wang, Z. Li, Wearable and implantable triboelectric nanogenerators, Adv. Funct. Mater. 29 (2019), 1808820.

[25] M.M. Yuan, L. Cheng, Q. Xu, W.W. Wu, S. Bai, L. Gu, Z. Wang, J. Lu, H.P. Li, Y. Qin, T. Jing, Z.L. Wang, Biocompatible nanogenerators through high piezoelectric coefficient 0.5Ba(Zr0.2Ti0.8)O-3-0.5(Ba0.7Ca0.3)TiO3 nanowires for in-vivo applications, Adv. Mater. 26 (2014) 7432–7437.

[26] X.L. Cheng, X. Xue, Y. Ma, M.D. Han, W. Zhang, Z.Y. Xu, H. Zhang, H.X. Zhang, Implantable and self-powered blood pressure monitoring based on a piezoelectric thinfilm: simulated, in vitro and in vivo studies, Nano Energy 22 (2016) 453–460.

[27] Z. Li, G.A. Zhu, R.S. Yang, A.C. Wang, Z.L. Wang, Muscle-driven in vivo nanogenerator, Adv. Mater. 22 (2010) 2534–2537.

[28] S. Azimi, A. Golabchi, A. Nekookar, S. Rabbani, M.H. Amiri, K. Asadi, M.M.J.N. E. Abolhasani, Self-powered cardiac pacemaker by piezoelectric polymer nanogenerator implant, Nano Energy 83 (2021), 105781.

[29] L. Dong, A.B. Closson, M. Oglesby, D. Escobedo, X.M. Han, Y. Nie, S.C. Huang, M. D. Feldman, Z. Chen, J.X.J. Zhang, In vivo cardiac power generation enabled by an integrated helical piezoelectric pacemaker lead, Nano Energy 66 (2019), 104085.

[30] Y. Ma, Q. Zheng, Y. Liu, B.J. Shi, X. Xue, W.P. Ji, Z. Liu, Y.M. Jin, Y. Zou, Z. An, W. Zhang, X.X. Wang, W. Jiang, Z.Y. Xu, Z.L. Wang, Z. Li, H. Zhang, Self-powered, one-stop, and multifunctional implantable triboelectric active sensor for real-time biomedical monitoring, Nano Lett. 16 (2016) 6042–6051.

[31] Z.R. Yi, F. Xie, Y.W. Tian, N. Li, X.X. Dong, Y. Ma, Y. Huang, Y.L. Hu, X.B. Xu, D. Qu, X.L. Lang, Z.Y. Xu, J.Q. Liu, H. Zhang, B. Yang, A battery- and leadless heart-worn pacemaker strategy, Adv. Funct. Mater. 30 (2020), 2000477.

[32] N. Li, Z.R. Yi, Y. Ma, F. Xie, Y. Huang, Y.W. Tian, X.X. Dong, Y. Liu, X. Shao, Y. Li, L. Jin, J.Q. Liu, Z.Y. Xu, B. Yang, H. Zhang, Direct powering a real cardiac pacemaker by natural energy of a heartbeat, ACS Nano 13 (2019) 2822–2830.

[33] H. Ouyang, Z. Liu, N. Li, B.J. Shi, Y. Zou, F. Xie, Y. Ma, Z. Li, H. Li, Q. Zheng, X. C. Qu, Y.B. Fan, Z.L. Wang, H. Zhang, Z. Li, Symbiotic cardiac pacemaker, Nature Commun. 10 (2019) 1–10.

[34] Q. Zheng, H. Zhang, B.J. Shi, X. Xue, Z. Liu, Y.M. Jin, Y. Ma, Y. Zou, X.X. Wang, Z. An, W. Tang, W. Zhang, F. Yang, Y. Liu, X.L. Lang, Z.Y. Xu, Z. Li, Z.L. Wang, In vivo self-powered wireless cardiac monitoring via implantable triboelectric nanogenerator, ACS Nano 10 (2016) 6510–6518.

[35] C. Dagdeviren, B.D. Yang, Y.W. Su, P.L. Tran, P. Joe, E. Anderson, J. Xia, V. Doraiswamy, B. Dehdashti, X. Feng, B.W. Lu, R. Poston, Z. Khalpey, R. Ghaffari, Y.G. Huang, M.J. Slepian, J.A. Rogers, Conformal piezoelectric energy harvesting and storage from motions of the heart, lung, and diaphragm, Proc. Natl. Acad. Sci. USA 111 (2014) 1927–1932.

[36] C.K. Jeong, J.H. Han, H. Palneedi, H. Park, G.T. Hwang, B. Joung, S.G. Kim, H. J. Shin, I.S. Kang, J. Ryu, K.J. Lee, Comprehensive biocompatibility of nontoxic and high-output flexible energy harvester using lead-free piezoceramic thin film, Apl. Mater. 5 (2017), 074102.

[37] H. Ryu, H.-m Park, M.-K. Kim, B. Kim, H.S. Myoung, T.Y. Kim, H.-J. Yoon, S. S. Kwak, J. Kim, T.H. Hwang, Self-rechargeable cardiac pacemaker system with triboelectric nanogenerators, Nat. Commun. 12 (2021) 1–9.

[38] G.T. Hwang, H. Park, J.H. Lee, S. Oh, K.I. Park, M. Byun, H. Park, G. Ahn, C. K. Jeong, K. No, H. Kwon, S.G. Lee, B. Joung, K.J. Lee, Self-powered cardiac pacemaker enabled by flexible single crystalline PMN-PT piezoelectric energy harvester, Adv. Mater. 26 (2014) 4880–4887, 4880-+.

[39] J. Li, L. Kang, Y. Long, H. Wei, Y.H. Yu, Y.H. Wang, C.A. Ferreira, G. Yao, Z. Y. Zhang, C. Carlos, L. German, X.L. Lan, W.B. Cai, X.D. Wang, Implanted battery-free direct-current micro-power supply from in vivo breath energy harvesting, ACS Appl. Mater. Interfaces 10 (2018) 42030–42038.

[40] D.H. Kim, H.J. Shin, H. Lee, C.K. Jeong, H. Park, G.T. Hwang, H.Y. Lee, D.J. Joe, J. H. Han, S.H. Lee, J. Kim, B. Joung, K.J. Lee, In Vivo self-powered wireless transmission using biocompatible flexible energy harvesters, Adv. Funct. Mater. 27 (2017), 1700341.

[41] Z.Y. Zhang, C.H. Yao, Y.H. Yu, Z.L. Hong, M.J. Zhi, X.D. Wang, Mesoporous piezoelectric polymer composite films with tunable mechanical modulus for harvesting energy from liquid pressure fluctuation, Adv. Funct. Mater. 26 (2016) 6760–6765.

[42] D.J. Jiang, B.J. Shi, H. Ouyang, Y.B. Fan, Z.L. Wang, Z. Li, Emerging implantable energy harvesters and self-powered implantable medical electronics, ACS Nano 14 (2020) 6436–6448.

[43] Q. Zheng, Q.Z. Tang, Z.L. Wang, Z. Li, Self-powered cardiovascular electronic devices and systems, Nature Rev. Cardiol. 18 (2021) 7–21.

[44] J. Li, Y. Long, F. Yang, X. Wang, Respiration-driven triboelectric nanogenerators for biomedical applications, EcoMat 2 (2020), e12045.

[45] B. Shi, Z. Li, Y. Fan, Implantable energy-harvesting devices, Adv. Mater. 30 (2018), 1801511.

[46] D.D. Gutterman, Silent myocardial ischemia, Circ. J. 73 (2009) 785–797.

[47] J.H. Pope, T.P. Aufderheide, R. Ruthazer, R.H. Woolard, J.A. Feldman, J. R. Beshansky, J.L. Griffith, H.P. Selker, Missed diagnoses of acute cardiac ischemia in the emergency department, N. Engl. J. Med. 342 (2000) 1163–1170.

[48] A.S. Jaffe, J. Ravkilde, R. Roberts, U. Naslund, F.S. Apple, M. Galvani, H. Katus, It's time for a change to a troponin standard, Circulation 102 (2000) 1216–1220.

[49] A.H.B. Wu, F.S. Apple, W.B. Gibler, R.L. Jesse, M.M. Warshaw, R. Valdes, National academy of clinical biochemistry standards of laboratory practice: recommendations for the use of cardiac markers in coronary artery diseases, Clin. Chem. 45 (1999) 1104–1121.

[50] H.A. Katus, A. Remppis, F.J. Neumann, T. Scheffold, K.W. Diederich, G. Vinar, A. Noe, G. Matern, W. Kuebler, Diagnostic efficiency of troponin-t measurements in acute myocardial-infarction, Circulation 83 (1991) 902–912.

[51] M.B. Bastos, D. Burkhoff, J. Maly, J. Daemen, C.A. den Uil, K. Ameloot, M. Lenzen, F. Mahfoud, F. Zijlstra, J.J. Schreuder, N.M. Van Mieghem, Invasive left ventricle pressure-volume analysis: overview and practical clinical implications, Eur. Heart J. 41 (2020) 1286–1297.

[52] H. Suga, Ventricular energetics, Physiol. Rev. 70 (1990) 247–277.

[53] Li Jun, Wang Xudong, Materials Perspectives for Self-Powered Cardiac Implantable Electronic Devices towards Clinical Translation, Accounts of Materials Research (2021), https://doi.org/10.1021/accountsmr.1c00078.